Journal of Mechanics, 2021, **37**, 680–692
https://doi.org/10.1093/jom/ufab033
Regular Article

IGA-PD penalty-based coupling for immersed air-blast fluid–structure interaction: a simple and effective solution for fracture and fragmentation

Masoud Behzadinasab[1], Michael Hillman[2] and Yuri Bazilevs[1,*]

[1]School of Engineering, Brown University, Providence, RI, United States
[2]Department of Civil and Environmental Engineering, The Pennsylvania State University, University Park, PA, United States

*Corresponding author: yuri_bazilevs@brown.edu

ABSTRACT

We present a novel formulation for the immersed coupling of isogeometric analysis and peridynamics for the simulation of fluid–structure interaction (FSI). We focus on air-blast FSI and address the computational challenges of immersed FSI methods in the simulation of fracture and fragmentation by developing a weakly volume-coupled FSI formulation by means of a simple penalty approach. We show the mathematical formulation and present several numerical examples of inelastic ductile and brittle solids under blast loading that clearly demonstrate the power and robustness of the proposed methodology.

KEYWORDS: FSI, IGA, peridynamics, volumetric penalty

1 INTRODUCTION

The present work is a continuation of the efforts first reported in [1,2], where the first and third authors of the present paper formulated a framework for immersed fluid–structure interaction (FSI) with applications to air blast. The coupled FSI formulation utilized the weak forms of the governing fluid and structural mechanics equations and discretized the equations using two meshes: background and foreground. The coupled FSI kinematics was approximated using the basis functions defined on the background mesh, while the solid domain integration, tracking of the solid current configuration and storing of the solid internal history variables were carried out on the foreground mesh. This construction resulted in a monolithic FSI coupling without the mesh distortion issues that may arise in moving-mesh techniques. One of the key breakthroughs reported in [1,2] was a clear demonstration that the use of non-uniform rational B-splines (NURBS)-based isogeometric analysis (IGA) [3,4] resulted in the increased accuracy of the discrete solution. In particular, the higher-order accuracy and smoothness of the strain-rate approximation completely removed the well-known cell-crossing instability of the traditional material-point methods (MPMs) that are typically discretized using low-order C^0-continuous finite element method (FEM) [5,6].

While the resulting FSI framework and its IGA-based implementation present a very promising approach and a clear advance over the existing methods, it was pointed out in [7] that the proposed methodology could benefit from further improvements.

Discretizing the solid on the background domain precludes the direct use of the existing, well-established solid and structural mechanics solvers in the proposed FSI framework. This lack of modularity was recently addressed in [7], where the authors developed a strongly coupled FSI formulation that introduced linear constraints between the background and foreground discrete function spaces. The kinematic compatibility was enforced through the constraint on the solution spaces, while that same constraint on the test functions gave a consistent definition of the discrete structural force vector on the nodes (or control points in the case of IGA) of the background grid. The resulting formulation was successfully demonstrated on the coupling of IGA with a state-based peridynamic (PD) solid [8–10].

Constraining the foreground solid to the background fluid kinematics as in [7] gives the desired modularity together with monolithic coupling; however, the modeling of fracture and fragmentation in the immersed FSI simulations remains a challenge. While the foreground discretization such as PD can easily support discontinuous kinematic fields by locally breaking bonds between material points [11–19], the smooth background discretization of IGA [20–28] is not designed to excel in approximating discontinuous kinematics. Thus, constraining the foreground solution to its background counterpart results in an overly smooth foreground solution and, when coupled with continuum-damage (or phase-field [26,27]) approaches to model fracture and fragmentation, results in the size of damage zones that scales with that of the background mesh. As a result, unless the background mesh is sufficiently fine, the

Received: 16 November 2021; **Accepted:** 23 November 2021

damage bands appear to be artificially thick and often predict non-physical behavior, especially in the brittle fracture regime. The width of the damage zones may be reduced by using a finer background mesh, but with a significant increase in the computational costs.

In order to directly address the issue of modeling fracture and fragmentation, an alternative approach is needed where the coupling of background and foreground solutions is weakened, especially in the presence of damage growth and fracture propagation. To develop such a coupling strategy, we took inspiration from a recent work [29] where an elaborate volume coupling methodology using a Nitsche technique [30] was formulated in the context of composite materials with a complex microstructure. In the present effort, we develop a relatively simple weakly coupled formulation where we only retain the penalty terms of the volumetric Nitsche approach. The main goal here is to assess whether the concept of weak coupling, in our case of IGA and PD, is effective in addressing the challenges involved in the modeling of fracture and fragmentation in the immersed FSI. Although in the present work PD is used for the modeling of the solid on the foreground domain, other meshfree methods like reproducing kernel particle methods (RKPM) [31–33] may be naturally employed for that purpose.

The paper is outlined as follows. In Section 2, we summarize the governing equations of fluid and structural mechanics at the continuum level. In Section 3, we revisit the strongly-coupled FSI formulation from [7] and develop a new weakly coupled approach by means of a carefully designed volumetric penalty operator. In Section 4, several 2D numerical examples are presented to compare the performance of the strongly and weakly coupled immersed FSI formulations, to study the effect of the penalty parameter choices on the solution quality and to demonstrate the effectiveness of weakly coupled approaches in dealing with fracture and fragmentation in solids and structures subjected to blast loading. In Section 5, we make concluding remarks and outlines future research directions.

2 FLUID AND STRUCTURAL MECHANICS GOVERNING EQUATIONS

Let Ω denote the FSI problem domain. Let Ω^{f} and Ω^{s} denote the fluid and solid subdomains in the spatial configuration, with $\Omega^{\mathrm{f}} \bigcup \Omega^{\mathrm{s}} = \Omega$ and $\Omega^{\mathrm{f}} \bigcap \Omega^{\mathrm{s}} = \emptyset$.

The fluid mechanics problem is governed by the Navier–Stokes equations of compressible flows. The weak form of the fluid problem makes use of the following semilinear forms and linear functionals:

$$M^f_\omega(\mathbf{W},\mathbf{Y}) = \int_\omega \mathbf{W}\cdot\mathbf{A}_0^f\mathbf{Y}_{,t}\,\mathrm{d}\omega, \tag{1}$$

$$B^f_\omega(\mathbf{W},\mathbf{Y}) = \int_\omega \mathbf{W}\cdot\mathbf{A}_i^f\mathbf{Y}_{,i}\mathrm{d}\omega - \int_\omega \mathbf{W}_{,i}\cdot(\mathbf{F}_i^p-\mathbf{F}_i^d)\mathrm{d}\omega, \tag{2}$$

$$F^f_\omega(\mathbf{W}) = \int_\omega \mathbf{W}\cdot\mathbf{S}^f\mathrm{d}\omega + \int_{\Gamma_H^f}\mathbf{W}\cdot\mathbf{H}^f d\Gamma. \tag{3}$$

Here,

$$\mathbf{Y} = \begin{bmatrix} p \\ \mathbf{v} \\ T \end{bmatrix} \tag{4}$$

is a set of pressure-primitive variables [34,35], where p is the pressure, $\mathbf{v}$ is the material-particle velocity and T is the temperature. $\mathbf{Y}$ and $\mathbf{W}$ are the vector-valued trial and test functions, respectively, that are members of $\mathcal{S}$ and $\mathcal{V}$, the fluid problem trial and test function spaces, respectively. It is important to note that these spaces are defined on all of Ω. The fluid traction and heat flux boundary conditions are imposed on Γ_H^f, and $\mathbf{H}^f$ contains the prescribed values of these boundary conditions. $\mathbf{F}_i^p$ and $\mathbf{F}_i^d$ are the pressure and viscous/thermal fluxes, respectively, $\mathbf{S}$ is the volume source, and $\mathbf{A}_0$ and $\mathbf{A}_i$ are the Euler Jacobian matrices. (The reader is referred to [1] and references therein for further details.) The subscript ω is used to denote the domain of integration, comma denotes partial differentiation with respect to the spatial coordinates and $i = 1, \ldots, d$, where $d = 2, 3$ is the space dimension. The compressible-flow equations are complemented with the ideal gas law as the equation of state.

With the above definitions, following [1], the continuous weak form of the compressible flow problem may be stated as: find $\mathbf{Y} \in \mathcal{S}$, such that $\forall \mathbf{W} \in \mathcal{V}$,

$$M^f_{\Omega^f}(\mathbf{W},\mathbf{Y}) + B^f_{\Omega^f}(\mathbf{W},\mathbf{Y}) - F^f_{\Omega^f}(\mathbf{W}) = 0. \tag{5}$$

The structure is modeled as an isothermal large-deformation inelastic solid using the framework of correspondence-based PD. Let $\tilde{\mathcal{S}}$ and $\tilde{\mathcal{V}}$ denote the trial and test function spaces for the PD formulation defined on Ω^{s}. Assuming the Lagrangian form of the mass balance equation and no thermal coupling, the pressure and temperature slots of the trial $(\tilde{\mathbf{Y}})$ and test $(\tilde{\mathbf{W}})$ functions are set to zero, while the slots 2: $2 + (d-1)$ are occupied by the solid velocity trial functions $(\tilde{\mathbf{v}})$ and the momentum-equation test functions $(\tilde{\mathbf{w}})$, respectively. That is,

$$\tilde{\mathbf{Y}} = \begin{bmatrix} 0 \\ \tilde{\mathbf{v}} \\ 0 \end{bmatrix}, \tag{6}$$

and

$$\tilde{\mathbf{W}} = \begin{bmatrix} 0 \\ \tilde{\mathbf{w}} \\ 0 \end{bmatrix}. \tag{7}$$

Following [7], the semilinear forms and linear functionals employed in the the solid problem are:

$$\mathcal{M}^s_{\Omega^s}(\tilde{\mathbf{W}},\tilde{\mathbf{Y}}) = \int_{\Omega^s}\tilde{\mathbf{w}}\cdot\rho^s\dot{\tilde{\mathbf{v}}}\,\mathrm{d}\Omega^s, \tag{8}$$

$$\mathcal{B}^s_{\Omega^s}(\tilde{\mathbf{W}},\tilde{\mathbf{Y}}) = \int_{\Omega^s}\tilde{\mathbf{w}}\cdot\int_{\mathcal{H}}(\underline{\mathbf{T}}-\underline{\mathbf{T}}')\,\mathrm{d}\mathcal{H}\,\mathrm{d}\Omega^s, \tag{9}$$

and

$$\mathcal{F}^s_{\Omega^s}(\tilde{\mathbf{W}}) = \int_{\Omega^s}\tilde{\mathbf{w}}\cdot\mathbf{s}\,\mathrm{d}\Omega^s. \tag{10}$$

Here, ρ^s is the current-configuration solid mass density, $\mathbf{s}$ is the volumetric source term, and the overdot symbol is used to denote the material time derivative. The PD family set (or horizon) $\mathcal{H}(\mathbf{x})$ of the point $\mathbf{x}$ is defined as

$$\mathcal{H}(\mathbf{x}) = \{\mathbf{x}' \mid \mathbf{x}' \in \mathcal{H}(\mathbf{x}) \cap \Omega^s, \quad 0 < |\mathbf{x}'-\mathbf{x}| \le \delta\}, \tag{11}$$

where δ is the horizon size, $\langle \mathbf{x} - \mathbf{x}' \rangle$ denotes a PD bond between $\mathbf{x}$ and $\mathbf{x}'$, $\underline{\mathbf{T}} = \mathbf{T}\langle \mathbf{x} - \mathbf{x}' \rangle$ is the PD force state, with $\underline{\mathbf{T}}' = \mathbf{T}\langle \mathbf{x}' - \mathbf{x} \rangle$. Underscores are employed to mark the bond-associated fields.

In the correspondence, PD framework classical constitutive laws may be employed to evaluate the Cauchy stress at the bond level. For this, the spatial velocity gradient is computed using the integral form employed the reproducing kernel (RK) methods. The relationship between the force state $\underline{\mathbf{T}}$ and the Cauchy stress depends on the details of the velocity-gradient definition and evaluation. In the present work, we adopt the formulation detailed in [7], Appendix A, and the reader is encouraged to consult this reference as well as [10,36] for further information.

With the above definitions, the continuous, weak correspondence-based PD formulation of the solid becomes: find $\tilde{\mathbf{Y}} \in \tilde{\mathcal{S}}$, such that $\forall \tilde{\mathbf{W}} \in \tilde{\mathcal{V}}$,

$$\mathcal{M}^s_{\Omega^s}(\tilde{\mathbf{W}}, \tilde{\mathbf{Y}}) + \mathcal{B}^s_{\Omega^s}(\tilde{\mathbf{W}}, \tilde{\mathbf{Y}}) - \mathcal{F}^s_{\Omega^s}(\tilde{\mathbf{W}}) = 0. \tag{12}$$

3 COUPLED FSI FORMULATIONS IN A DISCRETE FORM

In this section, we present two discrete forms of the volume-coupled FSI problem. The first approach is presented recently in [7], where the FSI coupling is carried out by explicitly constraining the fluid and solid velocity degrees-of-freedom (DOFs). We refer to this approach as *strong coupling*. As an alternative, we also explore a *weak coupling* approach based on a volumetric penalty formulation.

In both cases, we first define the background-domain finite-dimensional trial- and test-function spaces $\mathcal{S}^h \subset \mathcal{S}$ and $\mathcal{V}^h \subset \mathcal{V}$, respectively. The members of $\mathcal{S}^h$ and $\mathcal{V}^h$ may be written as

$$\mathbf{Y}^h(\mathbf{x}) = \sum_{B=1}^{\mathcal{N}_{cp}} \mathbf{Y}_B N_B(\mathbf{x}) \tag{13}$$

and

$$\mathbf{W}^h(\mathbf{x}) = \sum_{A=1}^{\mathcal{N}_{cp}} \mathbf{W}_A N_A(\mathbf{x}), \tag{14}$$

where $\mathbf{Y}_B$ and $\mathbf{W}_A$ are the control-point DOFs and weights, respectively, $N(\mathbf{x})$'s are the B-Spline basis functions and $\mathcal{N}_{cp}$ is the dimension of the B-Spline space. We also define $\tilde{\mathcal{S}}^h$ and $\tilde{\mathcal{V}}^h$, the finite-dimensional trial and test function spaces, respectively, for the PD solid. The members of $\tilde{\mathcal{S}}^h$ and $\tilde{\mathcal{V}}^h$ may be written as:

$$\tilde{\mathbf{Y}}^h(\mathbf{x}) = \sum_{Q=1}^{\mathcal{N}_{mp}} \tilde{\mathbf{Y}}_Q \, \chi_Q(\mathbf{x}) \tag{15}$$

and

$$\tilde{\mathbf{W}}^h(\mathbf{x}) = \sum_{P=1}^{\mathcal{N}_{mp}} \tilde{\mathbf{W}}_P \, \chi_P(\mathbf{x}), \tag{16}$$

where $\mathcal{N}_{mp}$ is the number of material points or PD nodes representing the solid, $\tilde{\mathbf{Y}}_Q$'s and $\tilde{\mathbf{W}}_P$'s are the discrete nodal DOFs and weights, respectively, and $\chi_P(\mathbf{x})$ is a characteristic function of a PD node P that satisfies

$$\int_{\Omega^s} \chi_P(\mathbf{x}) \, \mathrm{d}\Omega^s = V_P, \tag{17}$$

where V_P is the local volume of the PD node.

For the strong coupling approach, we use nodal interpolation to relate the foreground PD and background IGA discrete function spaces as

$$\tilde{\mathbf{Y}}^h(\mathbf{x}) = \Pi \mathbf{Y}^h(\mathbf{x}) = \sum_{Q=1}^{\mathcal{N}_{mp}} \left(\sum_{B=1}^{\mathcal{N}_{cp}} \mathbf{Y}_B N_B(\mathbf{x}_Q) \right) \chi_Q(\mathbf{x}) \tag{18}$$

and

$$\tilde{\mathbf{W}}^h(\mathbf{x}) = \Pi \mathbf{W}^h(\mathbf{x}) = \sum_{P=1}^{\mathcal{N}_{mp}} \left(\sum_{A=1}^{\mathcal{N}_{cp}} \mathbf{W}_A N_A(\mathbf{x}_P) \right) \chi_P(\mathbf{x}). \tag{19}$$

With these definitions, the spatially discretized, immersed, strongly coupled FSI formulation may now be stated solely in terms of the background domain unknowns as: find $\mathbf{Y}^h \in \mathcal{S}^h$, such that $\forall \mathbf{W}^h \in \mathcal{V}^h$,

$$\begin{aligned} &M^f_\Omega(\mathbf{W}^h, \mathbf{Y}^h) + B^f_\Omega(\mathbf{W}^h, \mathbf{Y}^h) - F^f_\Omega(\mathbf{W}^h) + B^{st}_\Omega(\mathbf{W}^h, \mathbf{Y}^h) \\ &\quad + B^{dc}_\Omega(\mathbf{W}^h, \mathbf{Y}^h) + \mathcal{M}^s_{\Omega^s}(\tilde{\mathbf{W}}^h, \tilde{\mathbf{Y}}^h) + \mathcal{B}^s_{\Omega^s}(\tilde{\mathbf{W}}^h, \tilde{\mathbf{Y}}^h) \\ &\quad - \mathcal{F}^s_{\Omega^s}(\tilde{\mathbf{W}}^h) - (M^f_{\Omega^s}(\mathbf{W}^h, \mathbf{Y}^h) + B^f_{\Omega^s}(\mathbf{W}^h, \mathbf{Y}^h) \\ &\quad - F^f_{\Omega^s}(\mathbf{W}^h) + B^{st}_{\Omega^s}(\mathbf{W}^h, \mathbf{Y}^h) + B^{dc}_{\Omega^s}(\mathbf{W}^h, \mathbf{Y}^h)) \\ &\quad = 0. \end{aligned} \tag{20}$$

In the space-discrete case, we augment the Galerkin formulation of compressible flows with the Streamline Upwing Petrov Galerkin (SUPG) stabilization ($B^{st}_\Omega(\mathbf{W}^h, \mathbf{Y}^h)$) [37–40] and discontinuity-capturing ($B^{dc}_\Omega(\mathbf{W}^h, \mathbf{Y}^h)$) [41–44] operators to obtain a stable formulation in the regime of convection dominance and to provide additional dissipation in the shock regions. The detailed definition of these operators that are employed in the present work may be found in [34,45,46]. Finally, because numerical quadrature is not explicitly defined in the standalone fluid mechanics domain, the integrals over the fluid mechanics domain are carried out by computing the contributions over the full FSI domain and subtracting the contributions from the solid domain.

Remark 3.1. *Constraining the trial and test functions of the PD domain to that of the background domain results in the following algorithmic approach to the strong FSI coupling. At the beginning of the step, the background fluid solution $\mathbf{Y}^h$ is interpolated to the PD mesh using Eq. (18), resulting in the field $\tilde{\mathbf{Y}}^h$. At this stage, $\mathbf{Y}^h$ is used to evaluate the discrete residual vector (also often called the nodal force vector) for the background domain, while $\tilde{\mathbf{Y}}^h$ is used to evaluate the discrete residual vector for the foreground domain. The foreground-domain residual vector is then distributed to the background-domain DOFs using a linear transformation induced by Eq. (19). The reader is referred to [7] for the details of this transformation. At this stage, the background-DOF residuals are added, and the solution increment is computed on the background mesh. The procedure repeats if multiple passes per step are employed.*

Remark 3.2. *The resulting strong coupling methodology is similar to the classical immersed boundary [47] and immersed finite element [48] methods, but, unlike these techniques, it does not use* ad hoc *smoothed delta functions to distribute the foreground-domain residual vector to the background DOFs.*

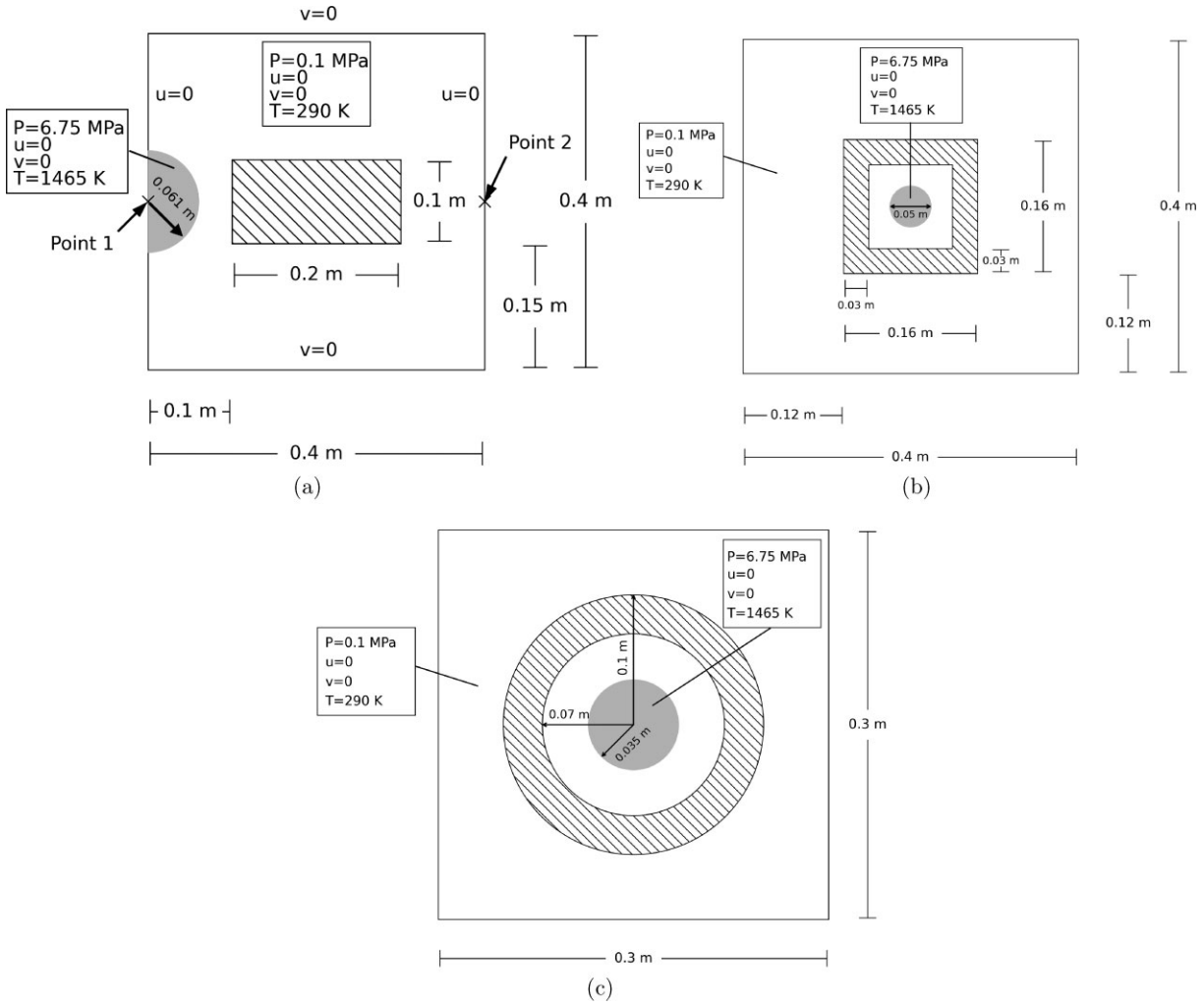

Figure 1 Descriptions of the problem setup and geometry for the examples computed. (a) Chamber detonation. (b) A hollow square block of ductile material subjected to internal explosion. (c) A hollow cylinder made of elastic, brittle material subjected to internal explosion.

The foreground-domain residual vector distribution on the background DOFs is defined consistently with the test-function constraints given by Eq. (19). This presents a clear benefit of using a variational formulation in the background domain, which is associated with the fluid mechanics part of the problem.

For the weak coupling approach, the fluid and structural equations are discretized independently and a volumetric penalty term is added to the formulation to penalize the deviation between the fluid and structural velocities. The resulting formulation is now stated in terms of both the background- and foreground-mesh unknowns as: find $\mathbf{Y}^h \in \mathcal{S}^h$ and $\tilde{\mathbf{Y}}^h \in \tilde{\mathcal{S}}^h$, such that for all $\mathbf{W}^h \in \mathcal{V}^h$ and $\tilde{\mathbf{W}}^h \in \tilde{\mathcal{V}}^h$,

$$\begin{aligned} &M^f_\Omega(\mathbf{W}^h, \mathbf{Y}^h) + B^f_\Omega(\mathbf{W}^h, \mathbf{Y}^h) - F^f_\Omega(\mathbf{W}^h) + B^{st}_\Omega(\mathbf{W}^h, \mathbf{Y}^h) \\ &\quad + B^{dc}_\Omega(\mathbf{W}^h, \mathbf{Y}^h) + \mathcal{M}^s_{\Omega^s}(\tilde{\mathbf{W}}^h, \tilde{\mathbf{Y}}^h) + \mathcal{B}^s_{\Omega^s}(\tilde{\mathbf{W}}^h, \tilde{\mathbf{Y}}^h) \\ &\quad - \mathcal{F}^s_{\Omega^s}(\tilde{\mathbf{W}}^h) + \int_{\Omega^s} (\mathbf{w}^h - \tilde{\mathbf{w}}^h) \cdot C_{\text{pen}} \, (\mathbf{v}^h - \tilde{\mathbf{v}}^h) \, \mathrm{d}\Omega^s \\ &\quad = 0. \end{aligned} \tag{21}$$

The penalty parameter C_{pen} in Eq. (21) needs a careful design to ensure a proper coupling between the fluid and structural systems and to not produce an overly stiff method with significant limitations on the stable time step size. It is also important to note that in the regions where the solid and fluid overlap, it is not necessary to generate an accurate fluid mechanics solution because, from the standpoint of the fluid problem, this region is completely fictitious. On the other hand, it is imperative that the solid solution is accurate and stable in this region since this is the actual solid domain. For these reasons, we choose C_{pen} to scale with the internal work terms of the solid formulation, which, with the aid of scaling arguments, yields the following definition:

$$C_{\text{pen}} = \beta \frac{E \Delta t}{h^2}. \tag{22}$$

Here E is the local elastic modulus, h is local mesh size, Δt is the time step size, and β is a dimensionless positive constant. The latter may be chosen just large enough to ensure that the penalty terms do not dominate the stable time step size, a common practice in contact and impact simulations using penalty

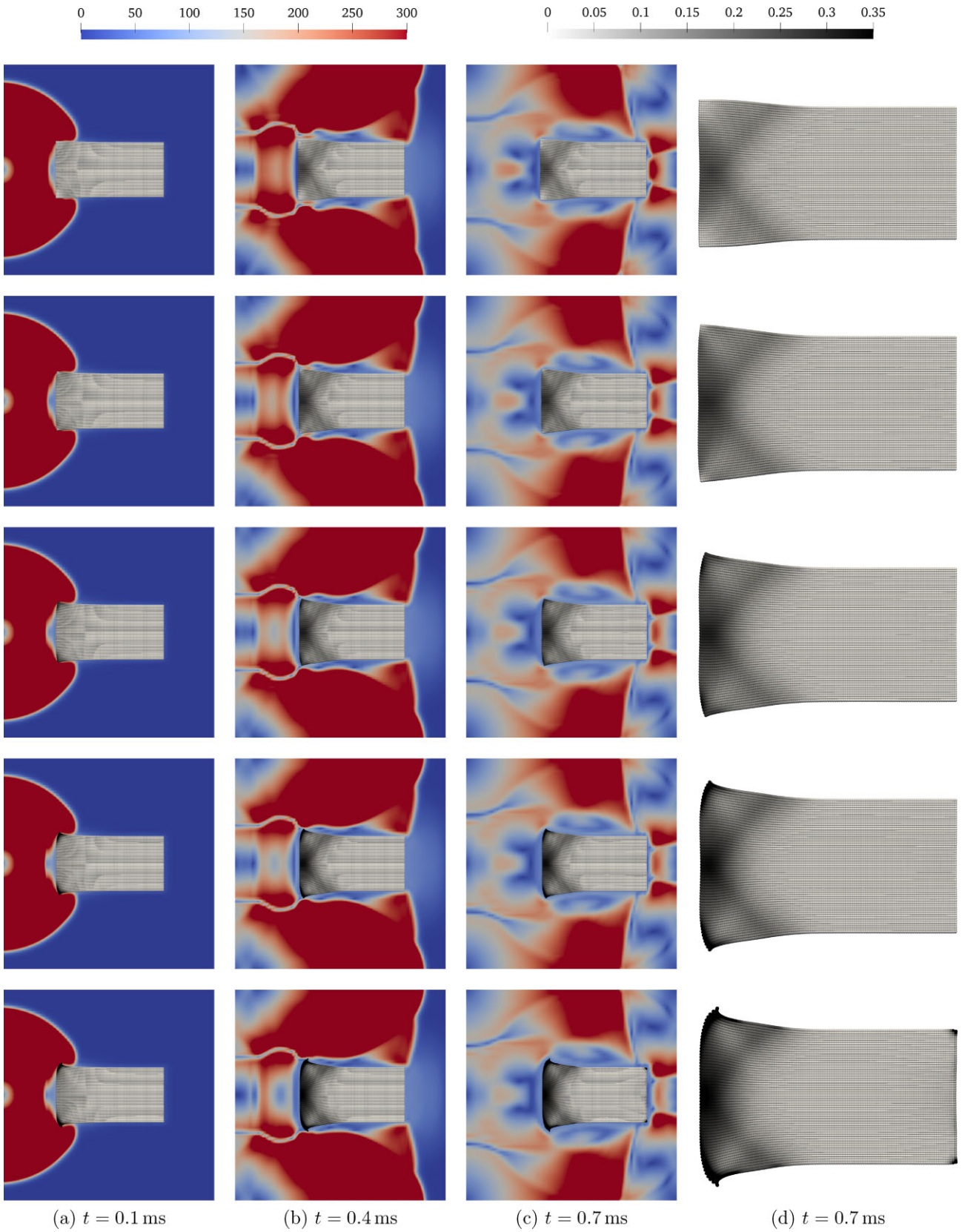

Figure 2 Chamber detonation problem. (a–c) Snapshots of air speed (in m/s) and solid plastic strain in the current configuration at different times for the finest mesh. From top to bottom, the individual rows correspond to $\beta = 1/3$, $\beta = 1.0$, $\beta = 3.0$, $\beta = 9.0$, and strong coupling, respectively. (d) Solid plastic strain at $t = 0.7$ ms.

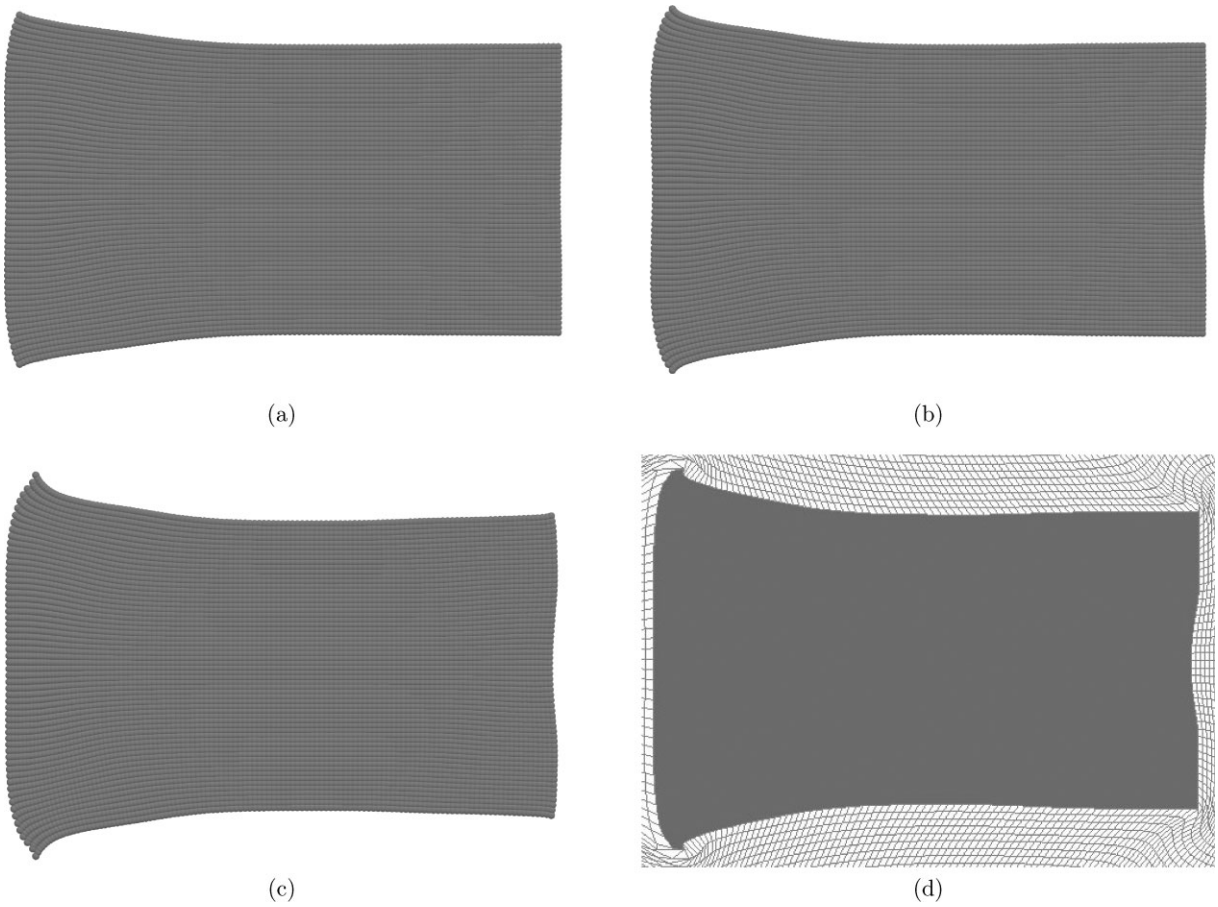

Figure 3 Chamber detonation problem. The solid deformed shape at $t = 1.5$ ms. (a) $\beta = 3.0$. (b) $\beta = 9.0$. (c) Strong coupling. (d) Conforming-mesh ALE result from [1].

methods (see [49–51]). In the case the material damage is modeled, we propose to further modify the penalty parameter as

$$C_{\text{pen}} = \beta \frac{(1-d)E\Delta t}{h^2}, \tag{23}$$

where d is a damage variable (or a phase field variable [26,27]) with $d = 1$ corresponding to a complete loss of material stiffness. We will examine the effects of the penalty parameter choice on the resulting coupled FSI solutions presented in the Numerical Examples section.

Remark 3.3. *The penalty parameter C_{pen} is present only in the last integral of Eq. (21). This integral is evaluated using numerical quadrature associated with the nodes of PD mesh, where the damage field is readily available.*

Remark 3.4. *The resulting weak coupling methodology is similar in structure to immersogeometric FSI (IMGA-FSI) [23,24,52,53], which is a new class of immersed FSI formulations that was developed for the coupling of incompressible flow with a Kirchhoff–Love shell [54] using a combination of penalty and Lagrange multiplier techniques. The present approach couples an IGA-based compressible flow formulation to a PD solid by means of a volumetric penalty only. A more elaborate Nitsche-like technique may be formulated in the future to make the approach more robust with respect to the selection of the penalty parameter.*

The resulting semi-discrete FSI equations, for both the strongly and weakly coupled formulations, are integrated in time using an explicit generalized-α technique [55] that is adopted for immersed FSI and detailed in [1].

4 NUMERICAL EXAMPLES

Three 2D numerical examples, shown in Fig. 1, are employed test and demonstrate the performance of the IGA-PD framework for FSI with a penalty-based coupling approach for blast loading and fragmentation applications. The material parameters and boundary and initial conditions for these examples may be found in [7]. C^1-continuous quadratic NURBS are used for the background IGA solution, while RK functions with quadratic consistency, rectangular support and bond-associative stabilization [56,10] are employed in the foreground PD formulation. The PD support size is chosen as $\delta = 2.5h$ [57], where h is the mesh size. In the examples involving damage, we report a *normalized solid mass loss*, which we define as

$$L_{\Omega^s} = \frac{\int_{\Omega^s} \chi(d)\, \rho^s \, \mathrm{d}\Omega^s}{\int_{\Omega^s} \rho^s \, \mathrm{d}\Omega^s}, \qquad \chi(d) = \begin{cases} 0 & \text{if } d < 0.99 \\ 1 & \text{otherwise} \end{cases}, \tag{24}$$

where d is the scalar damage field.

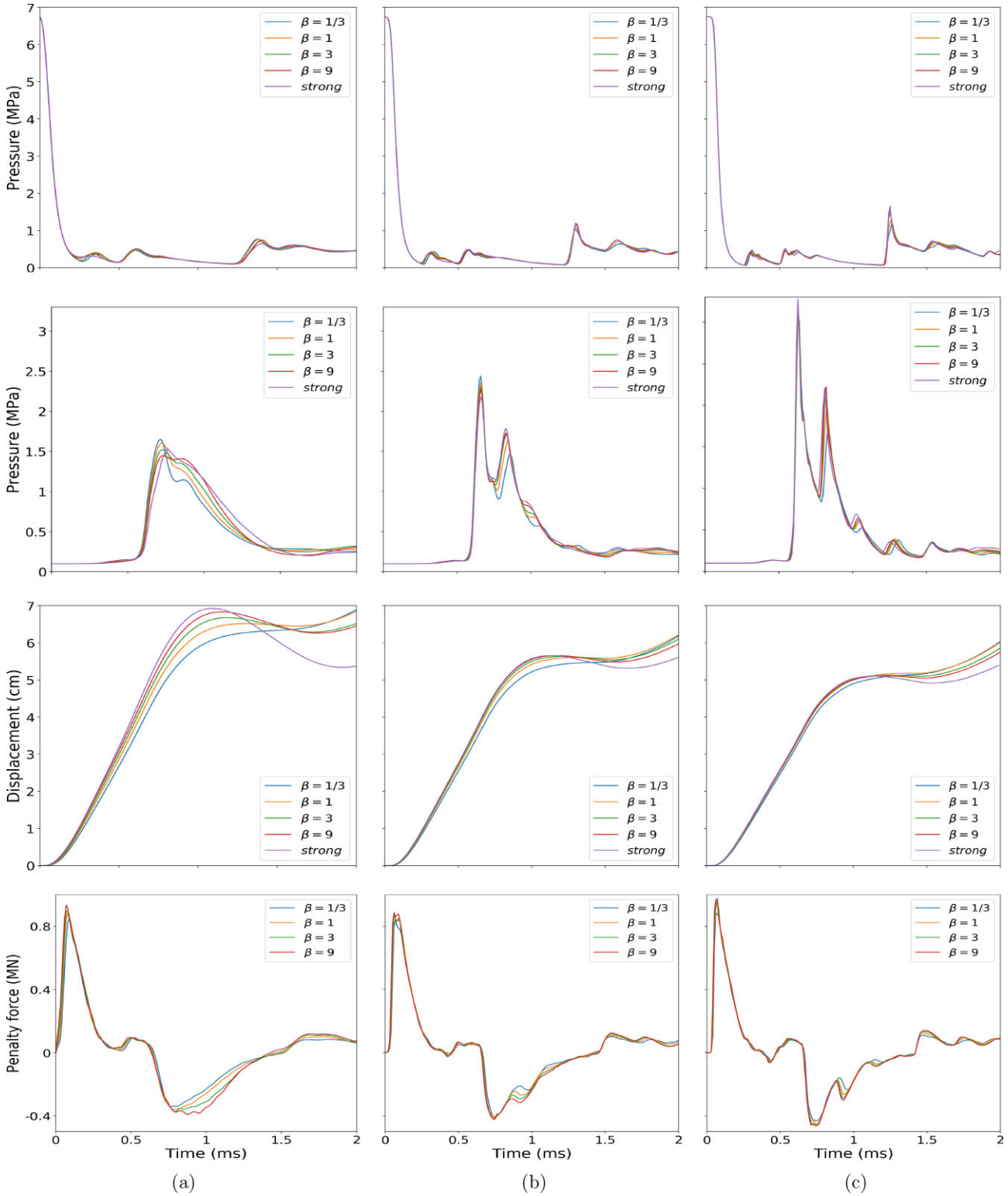

Figure 4 Chamber detonation problem. Comparison of the results for different discretization levels and coupling approaches. (a) Coarse mesh. (b) Medium mesh. (c) Fine mesh. From top to bottom, individual rows correspond to: (1) pressure at the center of detonation; (2) pressure at the center of the right wall; (3) horizontal displacement of the bar center of mass; and (4) horizontal component of the integrated penalty force.

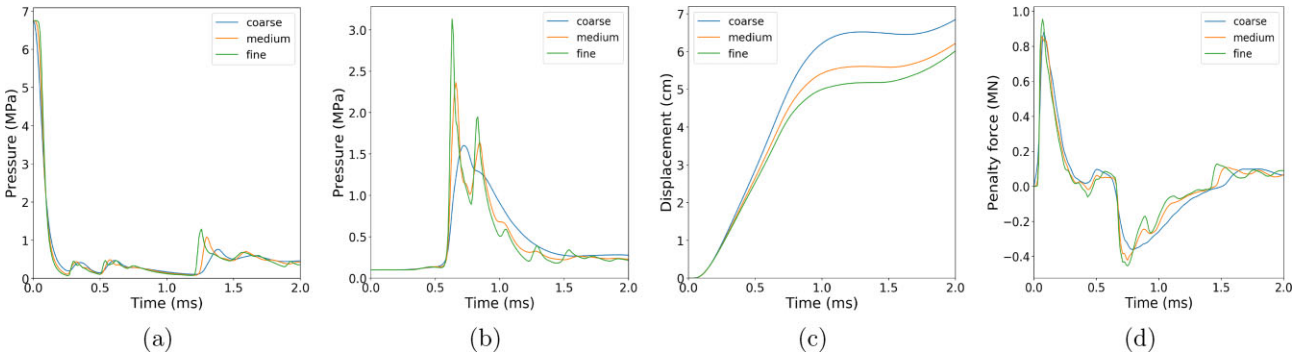

Figure 5 Chamber detonation problem. Comparison of the results for different discretization levels of $\beta = 1$. (1) Pressure at the center of detonation; (2) pressure at the center of the right wall; (3) horizontal displacement of the bar center of mass; and (4) horizontal component of the integrated penalty force.

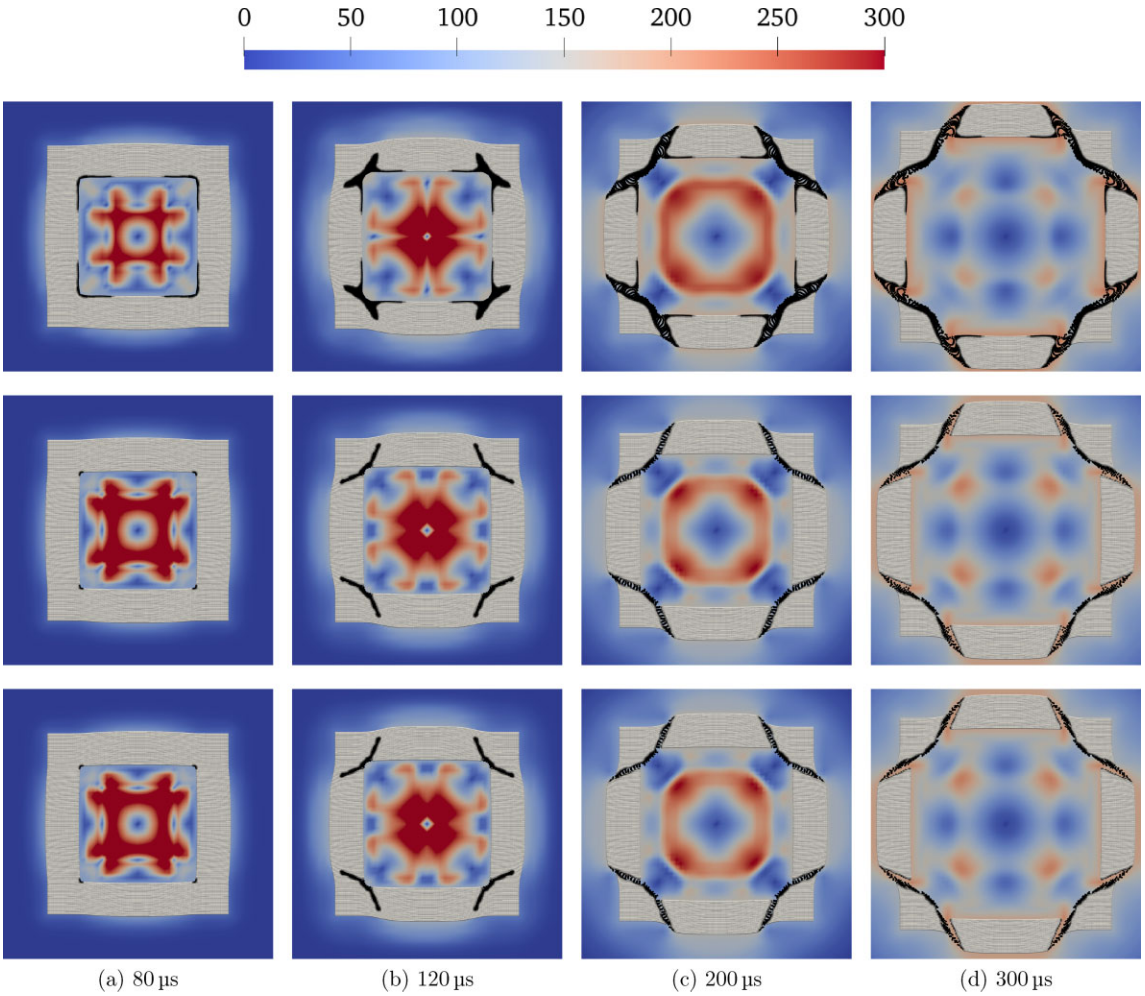

Figure 6 Ductile fracture problem. Snapshots of air speed (in m/s) and solid damage in the current configuration at different stages during the simulation for the finest mesh. Top, middle and bottom rows correspond to strong coupling, weak coupling without damage in the penalty stiffness, and weak coupling with damage in the penalty stiffness, respectively.

4.1 Chamber detonation

The problem setup is shown in Fig. 1a. We carry out the weakly coupled simulations using four non-dimensional penalty constants, $\beta = 1/3$, 1.0, 3.0, 9.0, and compare with the strongly coupled case. Three different discretizations are considered for each case: coarse - fluid: 20×20 elements; solid: 30×15 elements (PD nodes); medium - fluid: 40×40 elements; solid: 60×30 elements (PD nodes); fine - fluid: 80×80 elements; solid: 120×60 elements (PD nodes). In the PD case, each foreground element is replaced by a meshfree node at its centroid

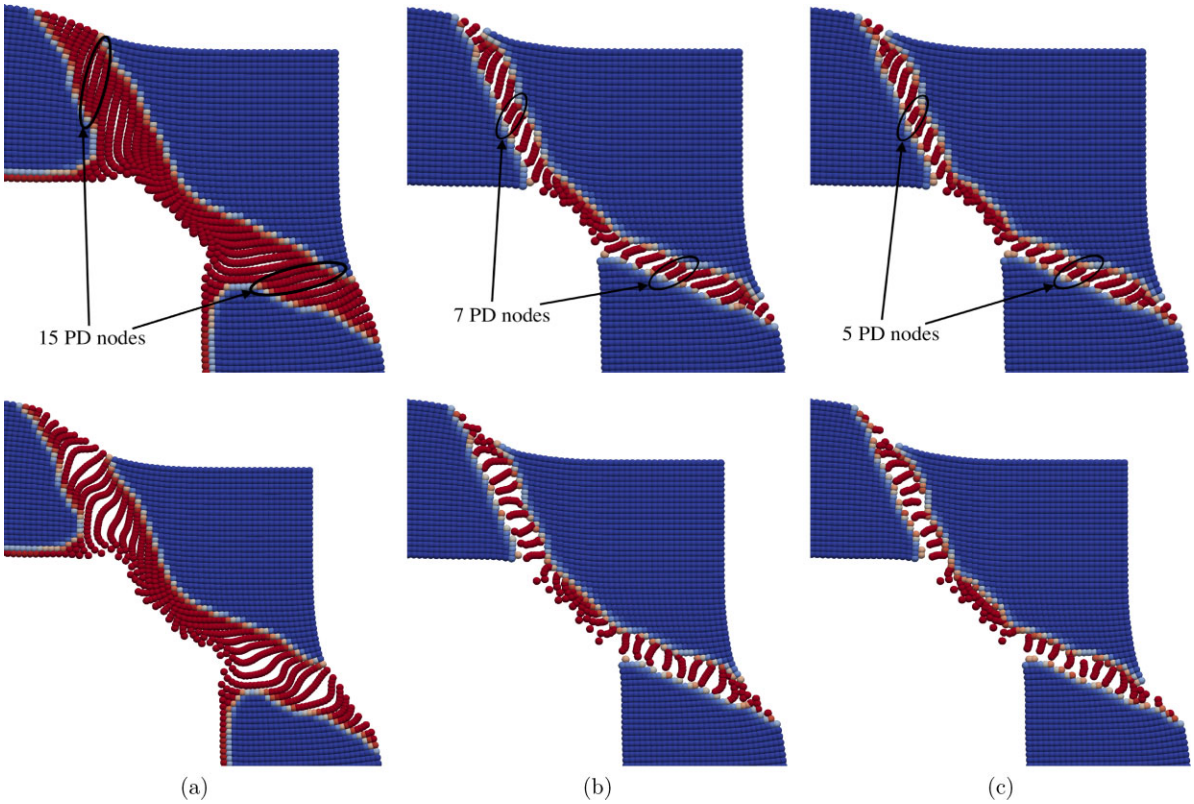

Figure 7 Ductile fracture problem. Comparison of solid damage for different coupling approaches. Zoomed-in view of the solutions for the finest mesh. Top and bottom rows correspond to 150 μs and 200 μs, respectively. The number of fully damaged PD nodes at the fracture interface is indicated. (a) Strong coupling. (b) Weak coupling without damage in the penalty stiffness. (c) Weak coupling with damage in the penalty stiffness.

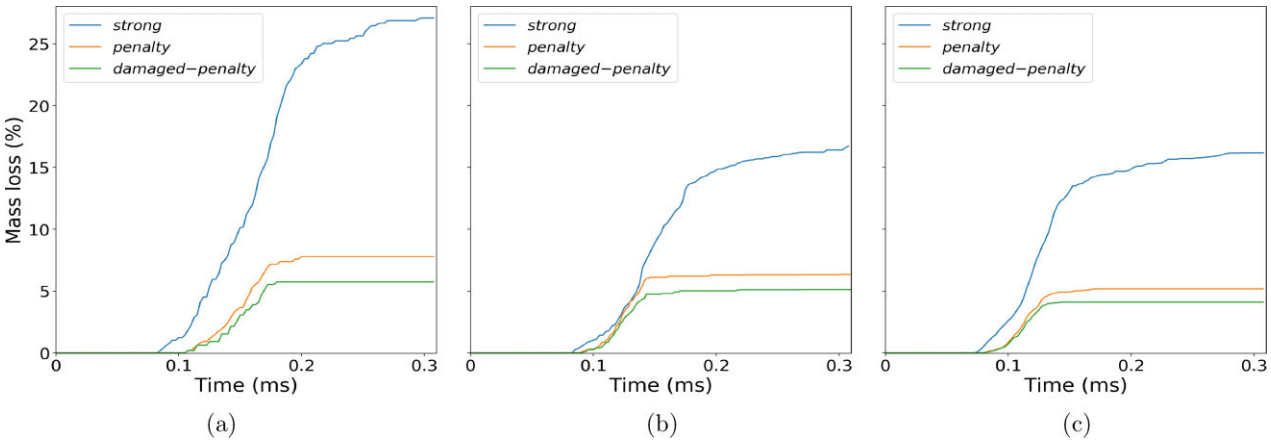

Figure 8 Ductile fracture problem. Comparison of the normalized solid mass loss for different coupling approaches and discretizations. (a) Coarse mesh. (b) Medium mesh. (c) Fine mesh. Here, *strong* indicates strong coupling, *penalty* indicates weak coupling without damage in the penalty stiffness and *damaged-penalty* indicates weak coupling with damage in the penalty stiffness.

with an equivalent volume. The time step size used for the coarse, medium and fine strongly coupled cases is 1 ms, 0.5 ms and 0.25 ms, respectively. The time step size used for all the weakly coupled cases is taken to be 8 times smaller than the corresponding values for the strongly coupled cases. This factor is chosen such that the simulations remain stable for the largest value of $\beta = 9.0$.

Air speed and solid plastic strain contours at several time instants are compared between the different cases computed on the finest mesh in Fig. 2. The fluid response appears to be very similar in all cases. As the penalty constant increases, plastic contours in the solid domain become more pronounced, more so near the domain boundaries and, especially, at the corners. The strong coupling produces excessive deformation and

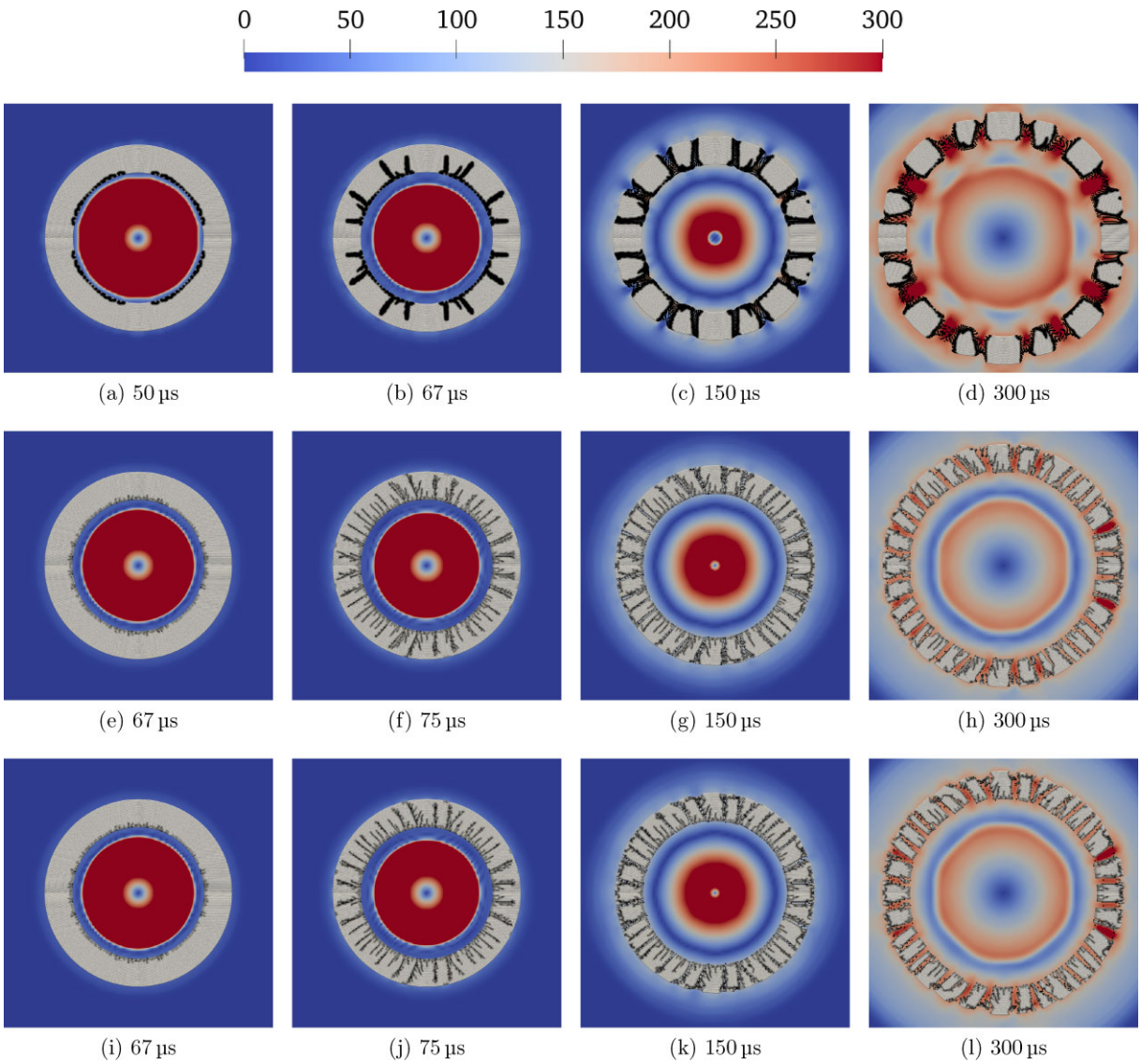

Figure 9 Brittle fracture problem. Snapshots of air speed (in m/s) and solid damage in the current configuration computed on the finest mesh. Top, middle and bottom rows correspond to strong coupling, weak coupling without damage in the penalty stiffness and weak coupling with damage in the penalty stiffness, respectively.

plastic straining at the domain corners because the discrete solution tries to accommodate high velocity gradients near the corners of the solid. Switching to weak coupling allows for some mismatch in the kinematics, and the domain corners experience little distortion, which is a real advantage of the proposed weak coupling.

In Fig. 3, the final shape of the bar (for the finest discretization) is compared for the weak and strong immersed FSI coupling approaches and the conforming-discretization arbitrary Lagrangian–Eulerian (ALE) simulation results taken from [1]. The agreement with the ALE results is quite good, especially for the higher penalty-constant case. Note the fluid mesh distortion in the vicinity of the corners for the ALE case. Figure 4 shows the time history of the pressure, the solid-object center-of-mass displacement, and the integrated penalty force on the solid in the x-direction for the 3 discretizations employed. Convergence with mesh refinement for all quantities may be inferred. In addition, the figure shows that the penalty force is not a strong function of the penalty constant value, which is an important observation on the robustness of the approach. Figure 5 shows the same quantities for the $\beta = 1.0$ case and for the 3 discretizations employed. We note that all the quantities clearly converge under mesh refinement, as well as the fact that the global penalty force is likewise not a strong function of the mesh size. This suggests that even using relatively coarse background meshes may result in an accurate total force the structure feels from the surrounding fluid.

4.2 Ductile solid subjected to internal explosion

The problem setup is shown in Fig. 1b. To simulate ductile fracture, a plasticity-driven failure approach described in [10,36] is employed with $\bar{\epsilon}^P_{\text{th}} = 0.18$ and $\bar{\epsilon}^P_{\text{cr}} = 0.2$. The background domain and foreground solid are discretized uniformly. Three

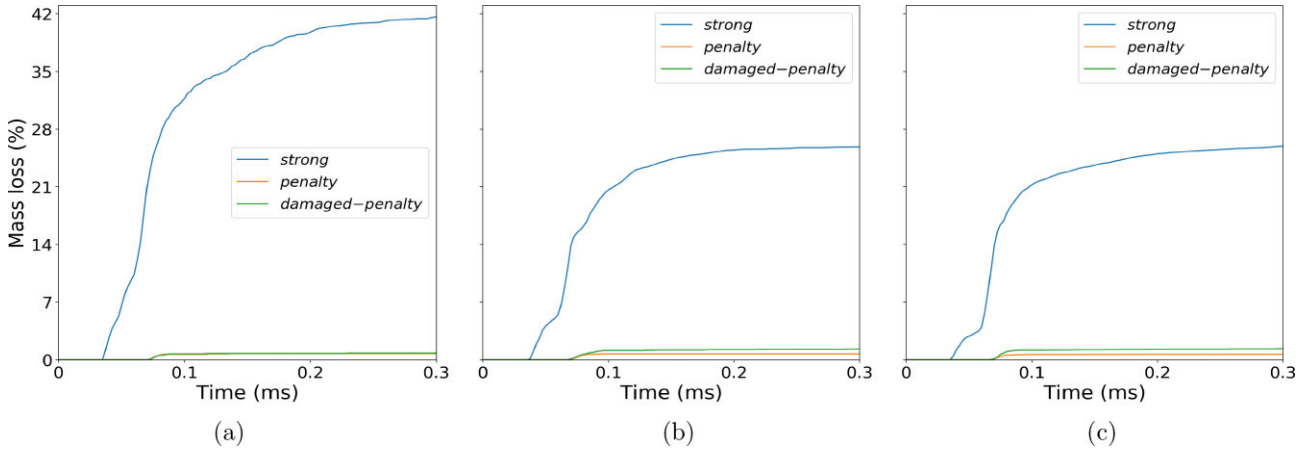

Figure 10 Brittle fracture problem. Normalized solid mass loss for different coupling approaches and discretizations: (a) coarse mesh; (b) medium mesh; and (c) fine mesh. Here, *strong* indicates strong coupling, *penalty* indicates weak coupling without damage in the penalty stiffness and *damaged-penalty* indicates weak coupling with damage in the penalty stiffness.

discretization levels are considered, with the solid node spacing of $h = 2$ mm, 1.5 mm and 1 mm, respectively. In each case, the fluid mesh size is set to four times that of the solid node spacing. The time step size used for the coarse, medium and fine strongly coupled cases is 0.4 μs, 0.3 μs and 0.2 μs, respectively. The time step used for the weakly coupled cases is four times smaller for the strongly coupled cases on the respective meshes. This choice is made to stably accommodate a penalty constant of $\beta = 1$ employed in the weakly coupled simulations. For the weakly coupled cases, we also examine the effect of adding the damage variable in the definition of the penalty parameter (see Section 3).

Figure 6 shows the results of the finest-mesh simulations, where the air speed is plotted on the background mesh while the damage field is plotted on the foreground PD nodes. In all cases, the fractures initiate at the interior corners, the locations of stress concentration, and show a very similar final pattern. However, the strongly coupled case exhibits much thicker damage bands and the structural response is sufficiently different to alter the fluid behavior as predicted by the strongly and weakly coupled cases. For the weak coupling, the damage bands are much narrower and, as a result, the fractures are much sharper. Figure 7 examines the thickness of the damage band in more detail and compares the results of the strong coupling to the weak coupling, with and without the damage variable affecting the penalty stiffness. The results with the damage variable affecting the penalty stiffness correspond to the sharpest and cleanest fracture. The time history of the normalized solid mass loss is plotted in Fig. 8 and gives a quantitative confirmation of the observations in Figs 6 and 7.

4.3 Brittle solid subjected to internal explosion

The problem setup is shown in Fig. 1c. To simulate brittle fracture using the bond-associative damage model [10,36], the maximum principal stress failure criterion is used with the critical stress $\sigma_{cr} = 3$ GPa. A PD bond is broken once its associated maximum principal stress exceeds σ_{cr}.

The background and foreground domains are discretized using a uniform rectangular mesh and a semi-uniform nodal spacing (uniform along the θ-direction), respectively. We again consider three meshes, with the solid node spacing of $h = 2$, 1.5 and 1 mm. The fluid mesh size is set to three times that of the solid node spacing in each case. The time step size for the coarse, medium and fine meshes in the strongly coupled case is set to 0.4 μs, 0.3 μs and 0.2 μs, respectively. The time step size used for the weakly coupled cases is four times smaller on the corresponding meshes. The penalty constant is set to $\beta = 1$.

Figure 9 shows the air speed on the background grid and the damage field on the PD nodes in the current configuration. Unlike in the ductile case, the blast wave shatters the brittle material into many small fragments as predicted by the weakly coupled simulations. However, in the strongly coupled case, the background mesh is not able to support such fine fragments and produces a much smaller number of larger-size chunks. This feature of the weakly coupled methods to enable the solid to fragment into small chunks that are not constrained in size to the resolution of the background grid is remarkable and presents a real breakthrough for the immersed FSI methods. We also note that the fragmentation results are very similar for the cases with and without damage dependence in the definition of the penalty parameter. The time history of the normalized solid mass loss reported in Fig. 10 shows a dramatic difference between the strongly and weakly coupled cases.

5 CONCLUSIONS

We developed a practical computational framework that is capable of capturing the mechanics of air blast coupled to solids and structures that undergo large, inelastic deformations, damage and fragmentation. The foundation for the proposed framework is an immersed FSI approach, which does not require explicit tracking of the fluid–structure interfaces and which has no limitations on the solid domain motion and topology. Weak forms of the fluid and structural mechanics equations are discretized on the background and foreground domains, respectively, and are coupled by means of a volumetric penalty operator, which is the main novelty of the proposed approach. We employ IGA based on NURBS in the background domain and

a correspondence-based PD solid in the foreground domain using the RK functions to define the non-local derivatives [57,58]. We feel that the combination of these numerical methodologies is particularly attractive for the problem class of interest due to the higher-order accuracy and smoothness of IGA and RK, the benefits of using immersed methodology in handling the fluid–structure interfaces and coupling, and the unique capabilities of PD for modeling fracture and fragmentation.

Using three numerical examples, the present work illustrates very clearly that strong coupling, a hallmark of immersed boundary methods and immersed finite element methods, while well suited for FSI with large solid deformations, is not an optimal approach for the modeling of fracture and fragmentation. On the other hand, weak coupling remains accurate for large-deformation FSI and enables the modeling of fracture and fragmentation with a lot less sticking, and with fragment sizes that are not constrained to the resolution of the background mesh. As such, the proposed methodology presents a real breakthrough in the application of immersed methods to FSI with fracture and fragmentation.

A likely explanation for the observed results is the fact that the volumetric penalty term attempts to minimize the error between the fluid and structural kinematics in the L_2-norm over the volume. L_2 is a weak norm that does not significantly penalize discontinuities or sharp gradients in the difference between the foreground and background solutions. As a result, the foreground solution is able to develop the discontinuities (i.e. fractures) that remain essentially undetected by the background mesh through the volumetric penalty operator. Conversely, in the strong coupling approach, any discontinuity generated on the foreground mesh is "overwritten" by the strong kinematics constraint to the smooth background grid that does not support solution discontinuities.

In the future, it may be worthwhile to investigate more elaborate volumetric Nitsche coupling approaches to reduce the dependence of the overall method performance, including the size of the stable time step in explicit simulations, on the choice of the penalty constant. However, one must be careful to not introduce stronger than necessary coupling and lose the benefits of the present approach.

ACKNOWLEDGEMENTS

The first and third authors were funded by the ONR grant no. N00014-21-1-2670. The second author was supported through the National Science Foundation award number 1826221.

REFERENCES

1. Bazilevs Y, Kamran K, Moutsanidis G, Benson DJ, Oñate E. A new formulation for air-blast fluid–structure interaction using an immersed approach. Part I: basic methodology and FEM-based simulations. *Computational Mechanics* 2017;**60**(1):83–100.
2. Bazilevs Y, Moutsanidis G, Bueno J, Kamran K, Kamensky D, Hillman MC, Gomez H, Chen JS. A new formulation for air-blast fluid–structure interaction using an immersed approach. Part II–coupling of IGA and meshfree discretizations. *Computational Mechanics* 2017;**60**(1):101–116.
3. Hughes TJ, Cottrell JA, Bazilevs Y. Isogeometric analysis: CAD, finite elements, NURBS, exact geometry and mesh refinement. *Computer Methods in Applied Mechanics and Engineering* 2005;**194**(39–41):4135–4195.
4. Cottrell JA, Hughes TJ, Bazilevs Y. *Isogeometric Analysis: Toward Integration of CAD and FEA*. Chichester: John Wiley & Sons, 2009.
5. Steffen M, Kirby RM, Berzins M. Analysis and reduction of quadrature errors in the material point method (MPM). *International Journal for Numerical Methods in Engineering* 2008;**76**(6):922–948.
6. Moutsanidis G, Long CC, Bazilevs Y. IGA-MPM: the isogeometric material point method. *Computer Methods in Applied Mechanics and Engineering* 2020;**372**:113346.
7. Behzadinasab M, Moutsanidis G, Trask N, Foster JT, Bazilevs Y. Coupling of IGA and peridynamics for air-blast fluid–structure interaction using an immersed approach. *Forces in Mechanics* 2021;**4**:100045.
8. Silling SA. Reformulation of elasticity theory for discontinuities and long-range forces. *Journal of the Mechanics and Physics of Solids* 2000;**48**(1):175–209.
9. Silling SA, Epton MA, Weckner O, Xu J, Askari E. Peridynamic states and constitutive modeling. *Journal of Elasticity* 2007;**88**(2):151–184.
10. Behzadinasab M, Foster JT. A semi-Lagrangian, constitutive correspondence framework for peridynamics. *Journal of the Mechanics and Physics of Solids* 2020;**137**:103862.
11. Bobaru F, Zhang G. Why do cracks branch? A peridynamic investigation of dynamic brittle fracture. *International Journal of Fracture* 2015;**196**(1–2):59–98.
12. Jafarzadeh S, Chen Z, Bobaru F. Peridynamic modeling of intergranular corrosion damage. *Journal of the Electrochemical Society* 2018;**165**(7):C362–C374.
13. Behzadinasab M, Vogler TJ, Peterson AM, Rahman R, Foster JT. Peridynamics modeling of a shock wave perturbation decay experiment in granular materials with intra-granular fracture. *Journal of Dynamic Behavior of Materials* 2018;**4**(4):529–542.
14. Kramer SL, Jones A, Mostafa A, Ravaji B et al., The third Sandia Fracture Challenge: predictions of ductile fracture in additively manufactured metal. *International Journal of Fracture* 2019;**218**(1):5–61.
15. Chen Z, Niazi S, Bobaru F. A peridynamic model for brittle damage and fracture in porous materials. *International Journal of Rock Mechanics and Mining Sciences* 2019;**122**:104059.
16. Behzadinasab M, Foster JT. The third Sandia fracture challenge: peridynamic blind prediction of ductile fracture characterization in additively manufactured metal. *International Journal of Fracture* 2019;**218**(1):97–109.
17. Gao C, Zhou Z, Li Z, Li L, Cheng S. Peridynamics simulation of surrounding rock damage characteristics during tunnel excavation. *Tunnelling and Underground Space Technology* 2020;**97**:103289.
18. Butt SN, Meschke G. Peridynamic analysis of dynamic fracture: influence of peridynamic horizon, dimensionality and specimen size. *Computational Mechanics* 2021;**67**(6):1719–1745.
19. Behzadinasab M, Alaydin M, Trask N, Bazilevs Y. A general-purpose, inelastic, rotation-free Kirchhoff-Love shell formulation for peridynamics. https://arxiv.org/abs/2107.13062.
20. Bazilevs Y, Calo VM, Zhang Y, Hughes TJ. Isogeometric fluid–structure interaction analysis with applications to arterial blood flow. *Computational Mechanics* 2006;**38**(4–5):310–322.
21. Bazilevs Y, Calo VM, Hughes TJ, Zhang Y. Isogeometric fluid-structure interaction: theory, algorithms, and computations. *Computational Mechanics* 2008;**43**(1):3–37.
22. Auricchio F, Calabro F, Hughes TJ, Reali A, Sangalli G. A simple algorithm for obtaining nearly optimal quadrature rules for NURBS-based isogeometric analysis. *Computer Methods in Applied Mechanics and Engineering* 2012;**249**:15–27.
23. Hsu MC, Kamensky D, Bazilevs Y, Sacks MS, Hughes TJ. Fluid–structure interaction analysis of bioprosthetic heart valves: significance of arterial wall deformation. *Computational Mechanics* 2014;**54**(4):1055–1071.
24. Kamensky D, Hsu MC, Schillinger D, Evans JA, Aggarwal A, Bazilevs Y, Sacks MS, Hughes TJ. An immersogeometric variational framework for fluid–structure interaction: application to bioprosthetic

heart valves. *Computer Methods in Applied Mechanics and Engineering* 2015;**284**:1005–1053.
25. Casquero H, Bona-Casas C, Gomez H. A NURBS-based immersed methodology for fluid–structure interaction. *Computer Methods in Applied Mechanics and Engineering* 2015;**284**:943–970.
26. Kamensky D, Moutsanidis G, Bazilevs Y. Hyperbolic phase field modeling of brittle fracture: Part I–theory and simulations. *Journal of the Mechanics and Physics of Solids* 2018;**121**:81–98.
27. Moutsanidis G, Kamensky D, Chen J, Bazilevs Y. Hyperbolic phase field modeling of brittle fracture: Part II–immersed IGA–RKPM coupling for air-blast–structure interaction. *Journal of the Mechanics and Physics of Solids* 2018;**121**:114–132.
28. Zhu Q, Xu F, Xu S, Hsu MC, Yan J. An immersogeometric formulation for free-surface flows with application to marine engineering problems. *Computer Methods in Applied Mechanics and Engineering* 2020;**361**:112748.
29. Wang J, Zhou G, Hillman M, Madra A, Bazilevs Y, Du J, Su K. Consistent immersed volumetric Nitsche methods for composite analysis. *Computer Methods in Applied Mechanics and Engineering* 2021;**385**:114042.
30. Nitsche J. Über ein Variationsprinzip zur Lösung von Dirichlet-Problemen bei Verwendung von Teilräumen, die keinen Randbedingungen unterworfen sind. In: *Abhandlungen aus dem mathematischen Seminar der Universität Hamburg*. vol. **36**. Springer, 1971, 9–15.
31. Liu WK, Jun S, Zhang YF. Reproducing kernel particle methods. *International Journal for Numerical Methods in Fluids* 1995;**20**(8–9):1081–1106.
32. Chen JS, Pan C, Wu CT, Liu WK. Reproducing kernel particle methods for large deformation analysis of non-linear structures. *Computer Methods in Applied Mechanics and Engineering* 1996;**139**(1–4):195–227.
33. Hillman M, Pasetto M, Zhou G. Generalized reproducing kernel peridynamics: unification of local and non-local meshfree methods, non-local derivative operations, and an arbitrary-order state-based peridynamic formulation. *Computational Particle Mechanics* 2020;7(2):435–469.
34. Hauke G, Hughes TJ. A comparative study of different sets of variables for solving compressible and incompressible flows. *Computer Methods in Applied Mechanics and Engineering* 1998;**153**(1–2):1–44.
35. Hauke G. Simple stabilizing matrices for the computation of compressible flows in primitive variables. *Computer Methods in Applied Mechanics and Engineering* 2001;**190**(51–52):6881–6893.
36. Behzadinasab M. Peridynamic modeling of large deformation and ductile fracture. PhD thesis, The University of Texas at Austin, 2020.
37. Brooks AN, Hughes TJ. Streamline upwind/Petrov-Galerkin formulations for convection dominated flows with particular emphasis on the incompressible Navier-Stokes equations. *Computer Methods in Applied Mechanics and Engineering* 1982;**32**(1–3):199–259.
38. Le Beau GJ, Ray S, Aliabadi S, Tezduyar T. SUPG finite element computation of compressible flows with the entropy and conservation variables formulations. *Computer Methods in Applied Mechanics and Engineering* 1993;**104**(3):397–422.
39. Tezduyar TE, Senga M. Stabilization and shock-capturing parameters in SUPG formulation of compressible flows. *Computer Methods in Applied Mechanics and Engineering* 2006;**195**(13–16):1621–1632.
40. Hughes TJ, Scovazzi G, Tezduyar TE. Stabilized methods for compressible flows. *Journal of Scientific Computing* 2010;**43**(3):343–368.
41. Hughes TJ, Mallet M, Akira M. A new finite element formulation for computational fluid dynamics: II. Beyond SUPG. *Computer Methods in Applied Mechanics and Engineering* 1986;**54**(3):341–355.
42. Tezduyar TE, Senga M, Vicker D. Computation of inviscid supersonic flows around cylinders and spheres with the SUPG formulation and *YZβ* shock-capturing. *Computational Mechanics* 2006;**38**(4):469–481.
43. Rispoli F, Saavedra R, Menichini F, Tezduyar TE. Computation of inviscid supersonic flows around cylinders and spheres with the V-SGS stabilization and *YZβ* shock-capturing. *Journal of Applied Mechanics* 2009;**76**(2):021209.
44. Rispoli F, Delibra G, Venturini P, Corsini A, Saavedra R, Tezduyar TE. Particle tracking and particle–shock interaction in compressible-flow computations with the V-SGS stabilization and *YZβ* shock-capturing. *Computational Mechanics* 2015;**55**(6):1201–1209.
45. Xu F, Moutsanidis G, Kamensky D, Hsu MC, Murugan M, Ghoshal A, Bazilevs Y. Compressible flows on moving domains: stabilized methods, weakly enforced essential boundary conditions, sliding interfaces, and application to gas-turbine modeling. *Computers & Fluids* 2017;**158**:201–220.
46. Bazilevs Y, Takizawa K, Wu MC, Kuraishi T, Avsar R, Xu Z, Tezduyar TE. Gas turbine computational flow and structure analysis with isogeometric discretization and a complex-geometry mesh generation method. *Computational Mechanics* 2021;**67**(1):57–84.
47. Peskin CS. Flow patterns around heart valves: a numerical method. *Journal of Computational Physics* 1972;**10**(2):252–271.
48. Zhang L, Gerstenberger A, Wang X, Liu WK. Immersed finite element method. *Computer Methods in Applied Mechanics and Engineering* 2004;**193**(21-22):2051–2067.
49. Benson DJ, Bazilevs Y, Hsu MC, Hughes TJ. Isogeometric shell analysis: the Reissner–Mindlin shell. *Computer Methods in Applied Mechanics and Engineering* 2010;**199**(5–8):276–289.
50. Benson DJ, Bazilevs Y, Hsu MC, Hughes TJ. A large deformation, rotation-free, isogeometric shell. *Computer Methods in Applied Mechanics and Engineering* 2011;**200**(13–16):1367–1378.
51. Alaydin MD, Benson DJ, Bazilevs Y. An updated Lagrangian framework for isogeometric Kirchhoff–Love thin-shell analysis. *Computer Methods in Applied Mechanics and Engineering* 2021;**384**:113977.
52. Kamensky D, Hsu MC, Yu Y, Evans JA, Sacks MS, Hughes TJ. Immersogeometric cardiovascular fluid–structure interaction analysis with divergence-conforming B-splines. *Computer Methods in Applied Mechanics and Engineering* 2017;**314**:408–472.
53. Kamensky D, Evans JA, Hsu MC, Bazilevs Y. Projection-based stabilization of interface Lagrange multipliers in immersogeometric fluid–thin structure interaction analysis, with application to heart valve modeling. *Computers & Mathematics with Applications* 2017;**74**(9):2068–2088.
54. Kiendl J, Bletzinger KU, Linhard J, Wüchner R. Isogeometric shell analysis with Kirchhoff–Love elements. *Computer Methods in Applied Mechanics and Engineering* 2009;**198**(49-52):3902–3914.
55. Chung J, Hulbert GM. A time integration algorithm for structural dynamics with improved numerical dissipation: the generalized-α method. *Journal of Applied Mechanics* 1993;**60**(2):371–375.
56. Breitzman T, Dayal K. Bond-level deformation gradients and energy averaging in peridynamics. *Journal of the Mechanics and Physics of Solids* 2018;**110**:192–204.
57. Behzadinasab M, Trask N, Bazilevs Y. A unified, stable and accurate meshfree framework for peridynamic correspondence modeling–part I: core methods. *Journal of Peridynamics and Nonlocal Modeling* 2021;**3**:24–45.
58. Behzadinasab M, Foster JT, Bazilevs Y. A unified, stable and accurate meshfree framework for peridynamic correspondence modeling–part II: wave propagation and enforcement of stress boundary conditions. *Journal of Peridynamics and Nonlocal Modeling* 2021;**3**:46–66.